chemosensors

MDPI

Article

Gas Sensors Based on Exfoliated g-C_3N_4 for CO_2 Detection

Ahmed Kotbi [1,2], Manal Benyoussef [1], El Mostafa Ressami [2], Michael Lejeune [1], Brahim Lakssir [2] and Mustapha Jouiad [1,*]

[1] Laboratory of Physics of Condensed Mater, University of Picardie Jules Verne, 80039 Amiens, France
[2] Moroccan Foundation for Advanced Science, Innovation and Research, Rabat 10100, Morocco
* Correspondence: mustapha.jouiad@u-picardie.fr

Abstract: We report on the investigation of graphitic carbon nitride (g-C_3N_4) for carbon dioxide (CO_2) sensor applications. g-C_3N_4 is prepared by the thermal polycondensation of thiourea and sprayed onto a substrate with interdigitated electrodes. The resulting sensor device exhibited a high sensitivity to CO_2 molecules of ~200 ppm, a high responsivity of ~730 ms at 40 °C and a full recovery time of 36 s. Furthermore, a set of various characterization measurements demonstrated the excellent stability of both the g-C_3N_4 nanosheets and the fabricated gas sensor device. Meanwhile, density functional theory (DFT) calculations for the bulk and monolayer models, based on tri-s-triazine, revealed the optoelectronic properties of g-C_3N_4 and the interaction energy with CO_2, which is evaluated at −0.59 eV. This value indicates the very good affinity of g-C_3N_4 nanosheets to CO_2 molecules. Our findings shed light on the potential for g-C_3N_4 to be used for the development of high-performing gas sensor devices.

Keywords: graphitic carbon nitride (g-C_3N_4); density functional theory (DFT); tri-s-triazine; optoelectronic properties; CO_2 gas sensors

Citation: Kotbi, A.; Benyoussef, M.; Ressami, E.M.; Lejeune, M.; Lakssir, B.; Jouiad, M. Gas Sensors Based on Exfoliated g-C_3N_4 for CO_2 Detection. *Chemosensors* **2022**, *10*, 470. https://doi.org/10.3390/chemosensors10110470

Academic Editors: Kai Xu and Zhong Li

Received: 24 October 2022
Accepted: 8 November 2022
Published: 10 November 2022

1. Introduction

Natural and industrial air pollutions due to toxic gas emissions constitute one of the major threats to the environment, causing serious hazards to human health such as respiratory and cardiovascular diseases [1]. Hence, there is an urgent need to reduce these emissions by issuing strict government regulations [2] while developing materials that can detect these gases before they reach the atmosphere. For gas detection, two-dimensional (2D) materials appear among the emerging solutions for gas sensing [3,4]. Indeed, due to their high surface area and good electronic and optical properties, 2D materials have attracted great attention in several domains such as photocatalysis, photovoltaics and gas sensing [5]. Among 2D materials, graphitic carbon nitride g-C_3N_4 (gCN) has shown several advantages for the development of gas sensors at a low processing cost and with low toxicity and high stability [6,7]. Indeed, gCN exhibits a planar structure similar to graphene, where C and N are covalently bonded, and adjacent layers are linked together by Van Der Waals forces. gCN has a tri-s-triazine cyclic structure, and the strong covalent coupling between C and N atoms offers this material very a high chemical and thermal stability under ambient conditions [8]. In addition, gCN can be used as a non-toxic organic semiconductor material possessing a bandgap energy of ~2.7 eV [9,10], making it a suitable catalyst for hydrogen evolution reaction, energy storage, contaminant degradation, CO_2 reduction and gas sensing [11]. In gas sensing applications, the performance of single-layer gCN remains attractive for two main reasons: (1) its intrinsic vacancies provide gCN with natural pathways for gas diffusion, unlike the artificial defects introduced in the other 2D materials [12,13]; (2) its large specific surface area offers gCN a high gas adsorption capacity [14]. gCN is easily synthesized by the thermal polycondensation process from affordable precursors such as thiourea (CH_4N_2S) [15], melamine ($C_3H_6N_6$) [16], dicyan-

diamide ($C_2H_4N_4$) [17] and urea (CH_4N_2O) [18], suggesting that it is one of the most promising candidates for industrial scaling up for various applications.

In the present work, a step-by-step fabrication and characterization of gCN are carried out to explore the routes of obtaining pure gCN to be used for gas sensing applications and especially CO_2 detection. Moreover, first-principles calculations are also performed to determine the optoelectronic properties of gCN responsible for its outstanding CO_2 detection.

2. Materials and Methods

Thiourea (CH_4N_2S, 99% purity, Alfa Aesar A12828.0E) and chloroform ($CHCl_3$, 67-66-3) were obtained from Fisher Scientific (Waltham, MA, USA). A crucible of 100 mL (Cole Parmer, Vernon Hills, IL, USA) and a furnace (Carbolite Gero, AAF 1100, Hope, UK) were used to synthesize gCN. Fourier transform infrared (FTIR) spectroscopy was conducted using KBr discs on an ABB Bomem FTLA2000 spectrophotometer. Thermogravimetric analysis (TGA) was carried out under an air atmosphere on a TA Instrument Q500 thermal analyzer. The crystal structure of thiourea was determined using X-ray powder diffraction (XRD) recorded on a Bruker-D4 diffractometer operating with Cu Kα irradiation. The vibration modes were recorded using a micro-Raman Renishaw spectrometer using UV light excitation (325 nm). A scanning electron microscope (SEM) Quanta 200 FEG and Transmission Electron Microscope (TEM) Tecnai from Thermo Fisher Sientific were used to examine the microstructure of the samples. A Retsch Milling Sieving Assisting machine was used for powder grinding, and a Palmsens 4 electrical measurements station was used for electrical measurements. A micro-probe system from the Nextron company (Basel, Switzerland) was used for gas detection tests (Figure 1). This system allows in-situ measurements of electrical properties under different environmental conditions: vacuum, temperature and controlled gas flow. The full sensing measurement set up was fully controlled by integrated software from Nextron. All detection tests were carried out in a gray room with a controlled relative humidity of 47%.

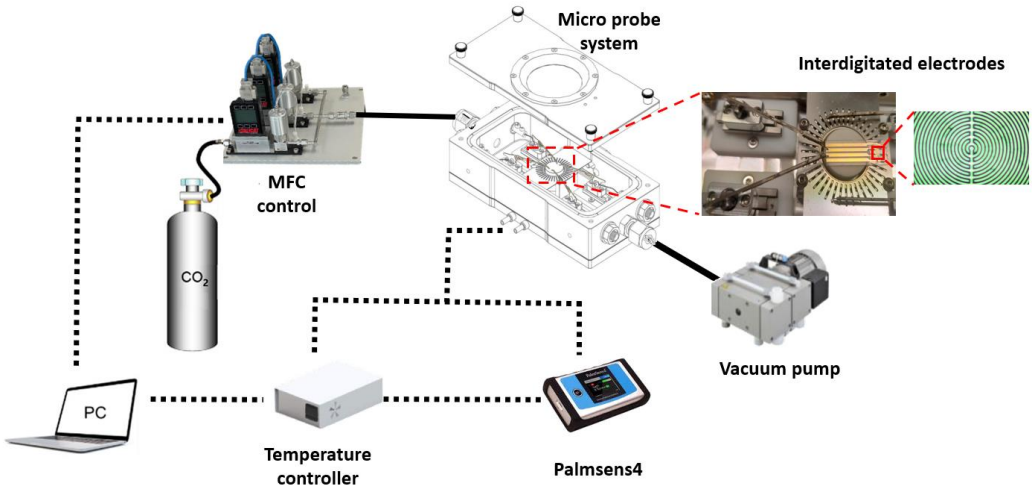

Figure 1. Sensing measurement set up used in this work.

The gCN nanosheets were elaborated by the thermal polycondensation of thiourea (CH_4N_2S). For this, 45 g of thiourea was placed in a closed alumina crucible and heated at 550 °C in a muffle furnace for 2 h at a heating rate of 5 °C/min. After natural cooling to room temperature, the obtained compound in the form of yellow powder was subsequently crashed using a ball milling machine. The powder was then exfoliated using ultrasound for 3 h in chloroform solution. The resulting solution was sprayed to form a thin film onto a substrate with interdigitated electrodes using the spray coating technique. The mixture of chloroform and gCN powder at 5.3×10^{-2} g/L concentration was sprayed at a 1 mL.mn^{-1} flow rate for 40 min while heating the substrate at 400 °C. During the whole spraying

process, the air pressure was maintained at 2 bar, and the spraying nozzle was placed 20 cm from the substrate.

3. Computational Method

The computed gCN has a hexagonal crystal structure, "space group P$\bar{6}$m2 (No. 187)". The valence electron configurations selected for C and N atoms are $2s^2$ $2p^2$ and $2s^2$ $2p^3$, respectively. The values of the relaxed lattice constants for bulk gCN are a = 7.135 Å and c = 7.040 Å. Figure 2a shows the 2 × 2 × 2 k-points used to obtain the band structure along the path H-K-Γ-M-L-H in the Brillouin zone. For the gCN monolayer (Figure 2b), 2 × 2 × 1 k-points were used, and a 15 Å vacuum space along the z-axis was added to isolate the gCN and prevent interactions between the adjacent layers.

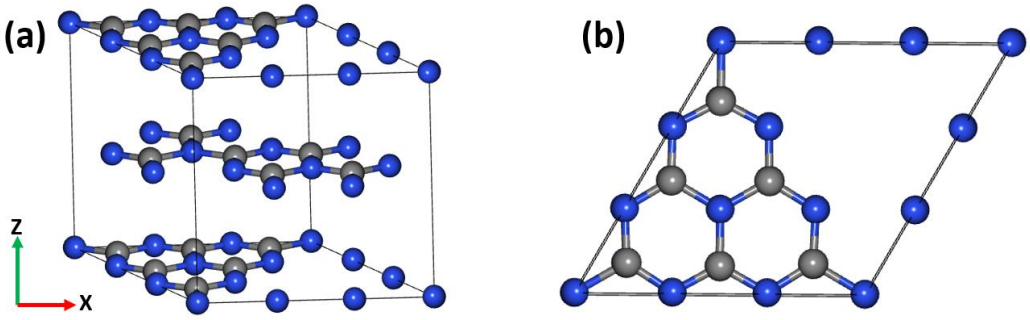

Figure 2. Geometric structure of heptazine-based gCN: (**a**) bulk; (**b**) monolayer. (C and N atoms are in black and blue respectively).

In the structure of gCN, the C and N atoms are represented, respectively, in black and in blue. The gCN monolayer model is obtained by removing other layers from the unit cell of the bulk gCN along the c direction. The structure of gCN includes eight N atoms and six C atoms for each layer. The energy cutoff of the plane basis was set to 500 eV. The calculations were performed using the Perdew–Burke–Ernzerhof (PBE) exchange-correlation function with generalized gradient approximation (GGA) and the Heyd–Scuseria–Ernzerhof (HSE06) hybrid function, implemented in Cambridge Sequential Total Energy Package (CASTEP) simulation software (22.1.1 version, CDG, Cambridge, UK).

4. Results and Discussion

4.1. Material Characterization

Figure 3 shows the TGA weight loss of thiourea. The first degradation is observed at ~200 °C with two endothermic peaks caused by the sublimation of thiourea. In the temperature range of 225–400 °C, there is a slight weight loss due to the thermal condensation of thiourea into triazine (melamine) and tri-s-triazine (heptazine). Tri-s-triazine could form by the intermolecular rearrangement of triazine. A second degradation is observed around ~450 °C, which corresponds to the onset of polymerization of gCN. The polycondensation of thiourea gives several products before the complete formation of gCN, such as triazine and tri-s-triazine [19].

Figure 4a shows the XRD diagram of gCN. The main peaks are located at 27.25° and 12.99°, indicating the formation of pure gCN. The XRD peak shapes confirm the graphitic stacking structure, highlighted by the presence of two peaks characteristic of gCN bulk and gCN nanosheets. The intense diffraction peak at 27.25° corresponds to the (002) reflection of the graphitic interlayer stacking structure of gCN, and the weak diffraction peak at 12.99° is attributed to the (100) plane of the planar repeating units in gCN. The crystallite size d is estimated using Scherrer's equation—$d = k.\lambda/\beta.\cos\theta$—to be ~9.28 nm and ~3.12 nm, respectively, for gCN bulk and nanosheets, where k is the shape constant (0.94), λ is the wavelength, θ is the Bragg angle and β is the peak full width at half-maximum. The XRD pattern of the polymeric gCN nanosheets indicates a graphitic structure with an interplanar stacking distance of aromatic units of ~0.33 nm.

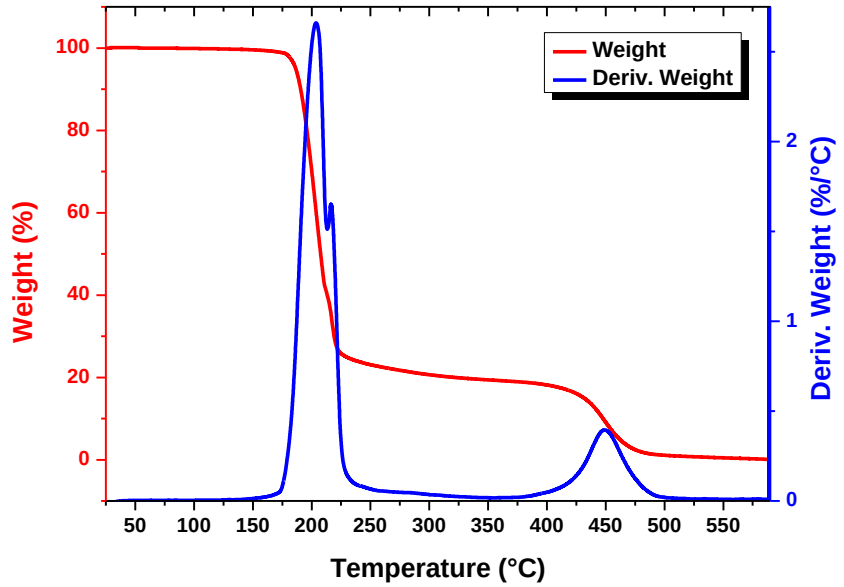

Figure 3. Weight loss of thiourea versus temperature and gCN formation.

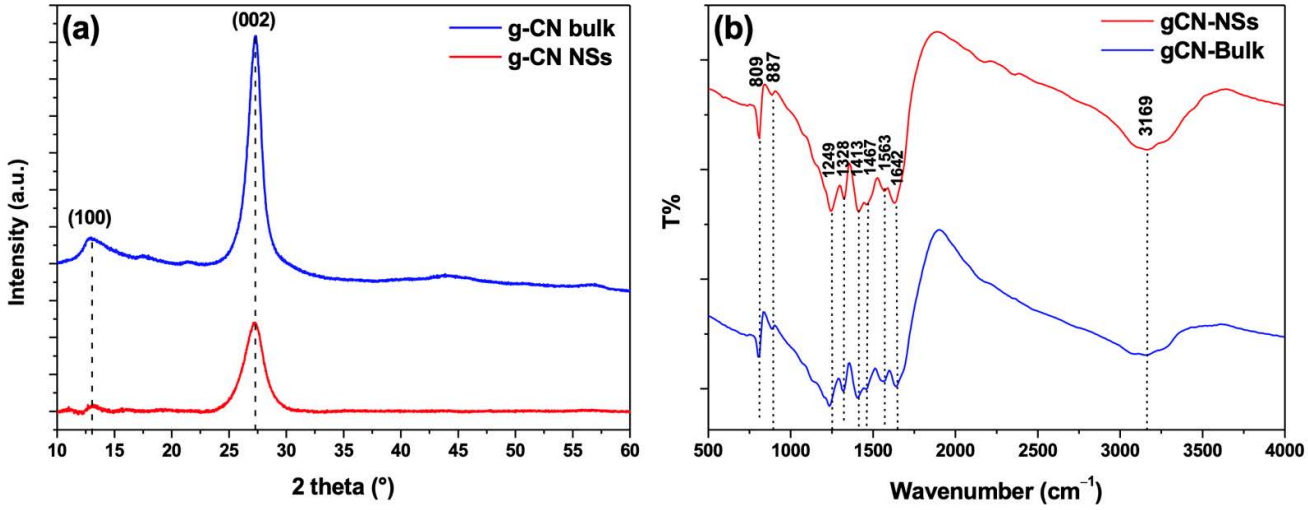

Figure 4. (**a**) X-ray diffraction diagram and (**b**) FTIR spectra of gCN bulk and nanosheets.

The FTIR spectra of the elaborated gCN are provided in Figure 4b. Two main peaks at 809 cm^{-1} and 887 cm^{-1} show the presence of s-triazine units, caused by the out-of-plane bending vibrations of the triazine ring. The peaks appearing at 1249 cm^{-1}, 1328 cm^{-1}, 1413 cm^{-1}, 1467 cm^{-1} and 1563 cm^{-1} are ascribed to the stretching vibrations of the C–N bonds in tri-s-triazine. The peak at 1642 cm^{-1} is due to the stretching vibration of the C=N bond in the heptazine units. The broadband absorption peak at 3169 cm^{-1} shows the stretching vibration of the N–H bond of NH and NH_2 groups, presumably caused by the incomplete polycondensation of gCN. As illustrated in Figure 4b, the FTIR spectra of gCN nanosheets and bulk gCN have the same chemical structure.

Note that, under visible light excitation, the Raman spectra of gCN present a single broad response, which is due to the strong fluorescence and photoluminescence effects occurring in the graphitic gCN phase when excited by visible light [20,21]. Hence, to better apprehend the Raman response, Raman analyses are conducted using UV laser excitation. Figure 5 depicts the temperature-dependent Raman spectra of the gCN sample collected in the frequency range of 300–1800 cm^{-1}. The Raman response at room temperature of gCN is in good agreement with the reported results [21–23]. Moreover, one can note the

presence of high intensity Raman modes at ~705 cm^{-1}, ~764 cm^{-1}, ~977 cm^{-1}, ~1113 cm^{-1}, ~1400 cm^{-1}, ~1483 cm^{-1}, ~1576 cm^{-1} and ~1620 cm^{-1}.

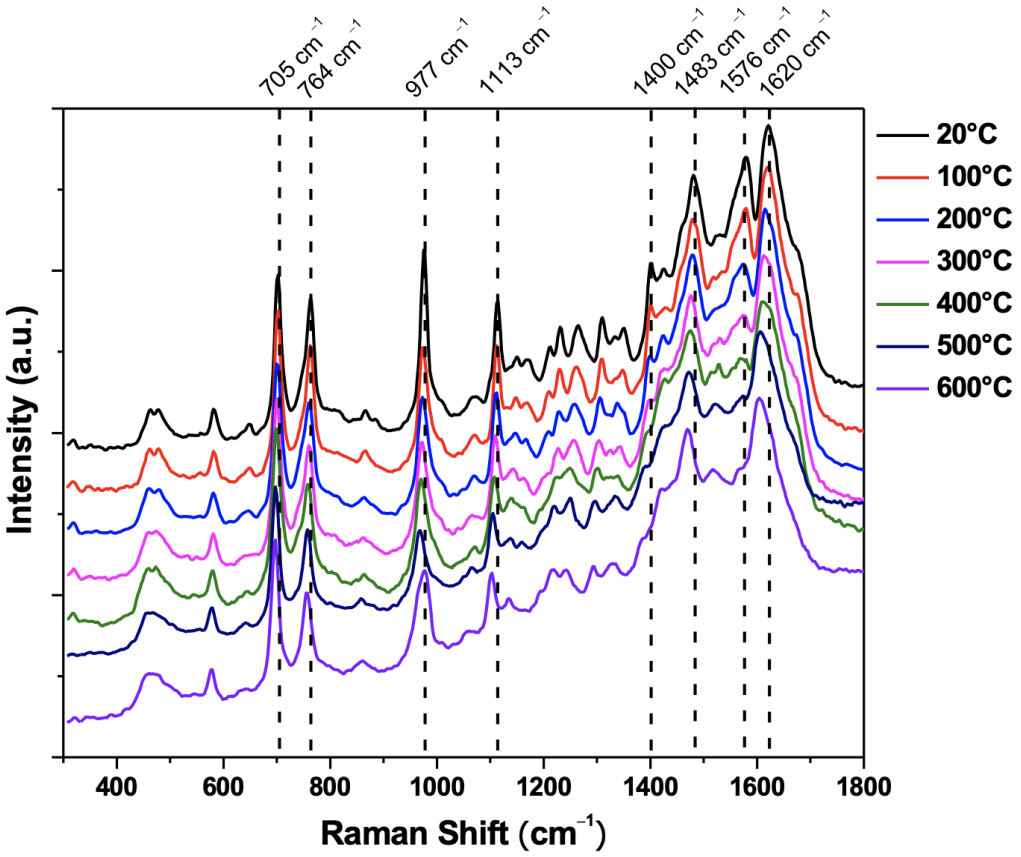

Figure 5. Temperature-dependent vibration modes of gCN excited with a UV laser, 325 nm.

The strong Raman vibration modes observed at 705 and 764 cm^{-1} are related to the intraplanar bending vibrations of the C−N=C linked heptazine units. Moreover, the mode at ~977 cm^{-1} was reported to be due to the symmetric N-breathing mode of the tri-s-triazine units [24]. These last modes are observed to present a blue shift as the temperature increases. Besides, the modes assigned to the D (1400 cm^{-1}) and G (1576 cm^{-1}) bands for the C sp^2 sites are also visible. The D band has an A_{1g} symmetry attributed to the breathing modes of C-sp^2 atoms in rings, and it is linked to structural defects, whereas the G band has E_{2g} symmetry involving the in-plane bond stretching motion of all C-sp^2 atoms and is linked to the degree of gCN graphitization [25,26]. As can also be seen, the temperature increase induced a weakening of the D and G Raman intensities ID and IG, respectively. To investigate the influence of the temperature change on the gCN structural distortions, the D and G bands' intensity ratio ID/IG was monitored. Indeed, our findings show that when the temperature increased from ambient to 600 °C, the ID/IG ratio also increased. This is the signature of a high degree of structural distortion in the gCN. In addition, all vibrational modes are seen to downshift at lower frequencies with increasing temperature. Of particular interest, these results concur with a high thermal stability of our elaborated gCN nanosheets for temperatures as high as 600 °C since no gCN degradation was registered.

The microstructures of elaborated gCN were analyzed by SEM and TEM, and the respective micrographs are depicted in Figure 6.

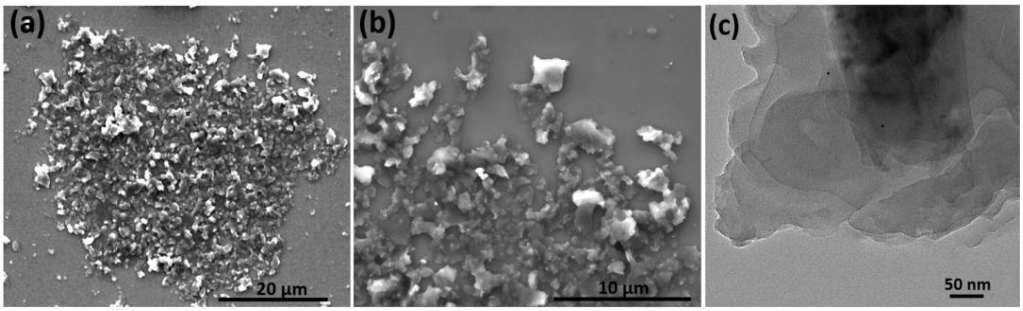

Figure 6. (**a**,**b**) Low and high magnification SEM images of gCN. (**c**) TEM image of layered gCN nanosheets.

The low and high magnification SEM images of dispersed nanosheets of gCN are given in Figure 6a,b, respectively. The nanosheet form is noticeable in these images, exhibiting a lateral size ranging from a few nanometers to a few micrometers. The TEM image shown in Figure 6c highlights the layered nanosheet morphology of the elaborated gCN. The size of the nanosheets is in the range of hundreds of nanometers. The stacking layers are evidenced; one can count four to five layers in Figure 6c.

4.2. Optical Properties

The band gap energy (E_g) of elaborated gCN is extracted from the absorption coefficient according to the model proposed by Tauc [27]:

$$\alpha h\nu = A(h\nu - E_g)^n, \quad (1)$$

where $h\nu$ is the photon energy, E_g is the band gap energy, A is a constant, and n is an exponent indicating the optical absorption nature. Plotting $(\alpha h\nu)^{1/2}$ against photon energy provides the indirect optical gap value. The band gap energy results are extracted here from the optical transmittance data of Figure 7a for the gCN bulk and monolayer and inserted in Figure 7b.

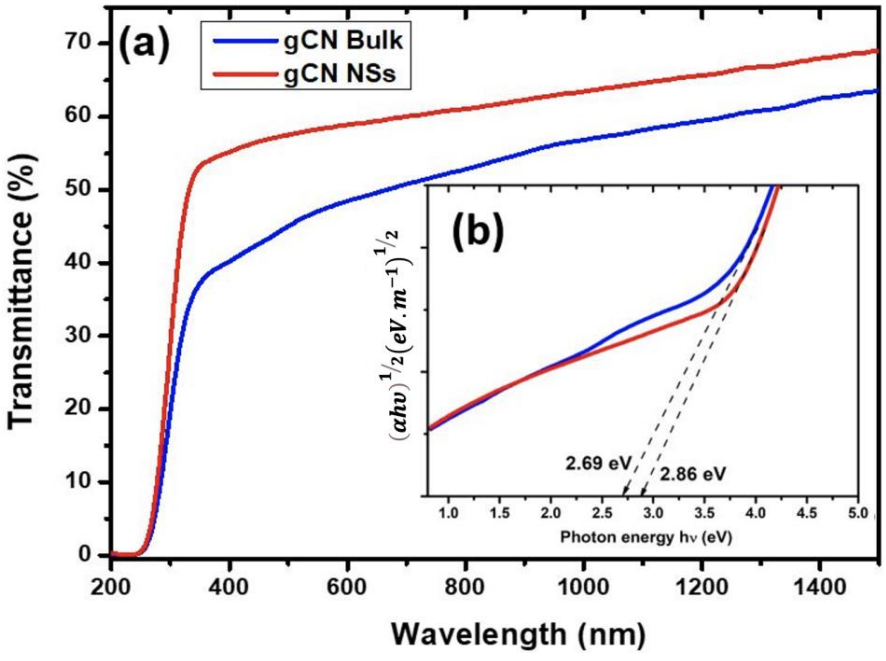

Figure 7. (**a**) Optical transmittance of both bulk and monolayer gCN, (**b**) $(\alpha h\nu)^{1/2}$ vs. photon energy for gCN bulk and monolayer and their respective band gap energy.

The gCN nanosheets exhibit higher transmittance in the full analyzed wavelength range of 300–1500 nm. The obtained band gap energy is 2.69 eV and 2.86 eV for the bulk and the nanosheets, respectively. These values are comparable to reported values [28–30].

4.3. Optoelectronic Properties

The band structures of gCN bulk and nanosheets, determined with different approximations, show that gCN has an indirect band gap with a minimum of the conduction band at point M of the Brillouin zone and the maximum of the valence band at point G of the Brillouin zone (e.g., Figure 8).

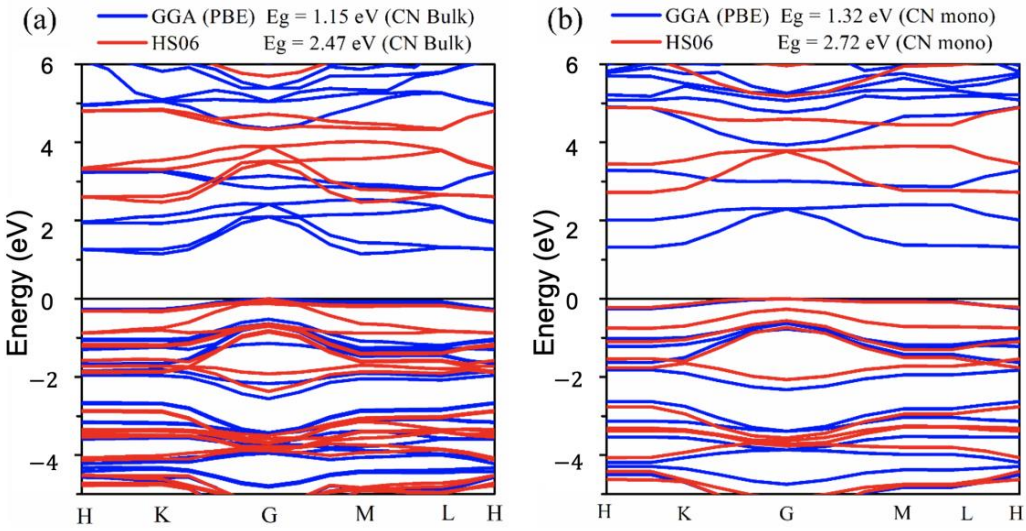

Figure 8. Band structure of gCN bulk (**a**) and gCN monolayer (**b**) obtained by DFT calculations using GGA-PBE (blue) and HS06 (red) approximations.

The computed band gap energies using GGA-PBE approximation show very low values of 1.15 eV and 1.32 eV for the gCN bulk and monolayer, respectively, which are surprisingly highly underestimated. However, using HSE06 approximation, the obtained band gap energies values are 2.47 eV and 2.72 eV for the gCN bulk abd gCN monolayer, respectively. These values are in agreement with the experimental results. We have gathered in the following Table 1 various reported band gap energies of the gCN bulk and monolayer computed using both approximations to be compared to experimental values.

Table 1. gCN band gap energy comparison—experimental and theoretical.

System	Theoretical "DFT" E_g (eV)	Approximation	Experimental E_g (eV)
gCN bulk	1.36 [31]; 1.41 [32]; 1.15 [this work]	GGA-PBE	2.51 [33]; 2.59 eV [34]
	2.73 [31]; 2.71 [6]; [35], 2.68 [36]; 2.80 [37]; 2.47 [this work]	HSE06	2.69 eV [this work]
gCN monolayer	1.59 [38] 1.32 [this work]	GGA-PBE	2.70 [39], 2.71 [40]
	2.76 [41], 2.93 [42], 2.96 [43], 2.97 [38], 3.20 [44], 3.22 [45], 4.02 [46] 2.72 [this work]	HSE06	2.86 eV [this work]

From this table, it is clear that the GGA-PBE approximation provides underestimated band gap energy values, as reported in various work, while the HSE06 approximation shows a very good agreement with the experimental results.

The total and partial densities of states (TDOS and PDOS) of the gCN bulk and monolayer are then computed using the HSE06 approximation and given in Figure 9a,b, respectively.

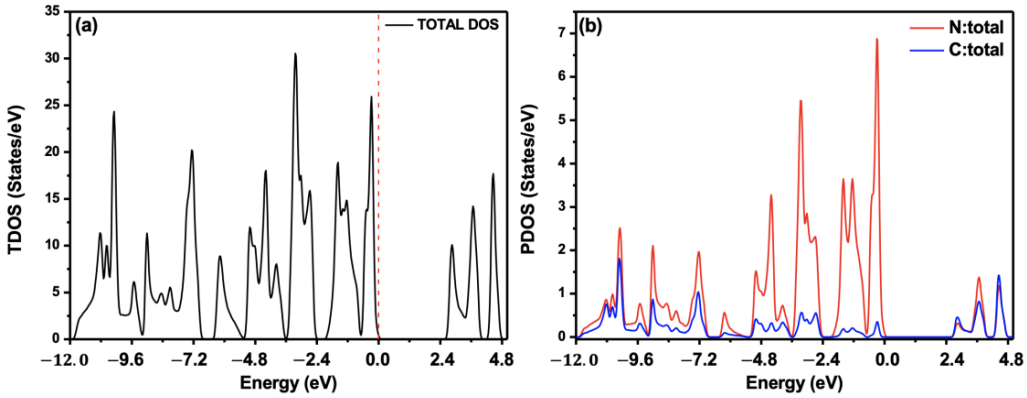

Figure 9. (**a**) Total density of states (TDOS) and (**b**) partial density of states (PDOS) plots of gCN bulk and monolayer.

TDOS provides the overall states of both N and C atoms, whereas PDOS permits us to segregate both constituents. Indeed, our PDOS results show that the energy band states near the Fermi energy in the valence band are mainly occupied by the electrons of the N atoms, and only a small contribution of the electrons is derived from C atoms. In contrast, the conduction band is mainly constituted of atomic orbitals of both N and C with a large contribution from the C atom. This band is dominated by a strong hybridization of the electrons of the N and C atoms. Hence, both atoms could participate in gCN interactions with volatile gas, providing more possible sites for gas detection.

Moreover, we have determined the adsorption energy (E_{ads}) between the CO_2 gas molecule and the gCN monolayer using GGA-PBE approximation [19]. The obtained adsorption energy of the system is calculated using the following relationship [19]:

$$E_{ads} = E_{gCN-CO2} - \left(E_{gCN} + E_{gas}\right), \quad (2)$$

where $E_{gCN-CO2}$ is the total energy of the adsorbed CO_2 molecules by the gCN surface, and E_{gCN} and E_{CO2} are, respectively, the total energies of gCN and a CO_2 molecule. A positive adsorption energy value indicates that the reaction is endothermic and therefore unstable and energetically unfavorable, while a negative value concurs with energetically favorable adsorption as the reaction is exothermic and thus stable. Table 2 shows the optimized structure of gCN while performing the adsorption calculations, including the distance between the CO_2 molecule and the gCN edge and the bond length.

Table 2. Structural comparisons after adsorption of CO_2 at the surface of gCN and their adsorption energy.

	Before Optimization	**Optimized Structure**
gCN-CO_2 configuration	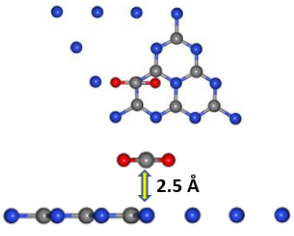	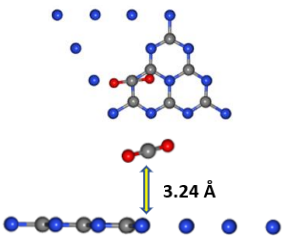
Angle (degree)	180	179.42
Bond length (Å)	1.181	1.172/1.170
Distance gCN–CO_2 (Å)	2.5	3.24
E_{ads} (eV)	−0.59	

Our finding revealed an adsorption energy value $E_{ad} = -0.59$ eV. This result indicates that the reaction is exothermic and therefore stable and energetically favorable. This is consistent with the high surface stability of gCN against CO_2 molecules, which could lead to its high reactivity and is beneficial to enhancing gCN sensing performances. From the above, one can notice that the elaborated gCN nanosheets are highly suitable for CO_2 sensing.

4.4. Gas Sensing Tests

In this work, we have used a resistive gas sensor based on a charge transfer process, in which the sensor acts as a charge donor [47]. Once the sensor device is exposed to CO_2 gas, it is assumed that the charge transfer reaction occurs in different directions between the sensor and the adsorbed gases. This results in changes in the resistance of the sensor [48]. Adsorption-based sensors use the change in resistance of the g-CN nanosheet caused by the adsorption of CO_2. A physical adsorption takes place at the g-CN–CO_2 interfaces, leading to a reduction of CO_2 to CO_2^- ; thus, electrons exchange, modifying the electrical performances of the material as per the following reaction [49]:

$$CO_{2\ (gas)} + e^- \leftrightarrow CO^-_{2(ads)},$$

To investigate the device recovery time dependent on temperature, we heated the gCN device to fully restore its base strength; then, we conducted CO_2 detection tests at 30 °C, 35 °C and 40 °C while monitoring the recovery time as shown in Figure 10.

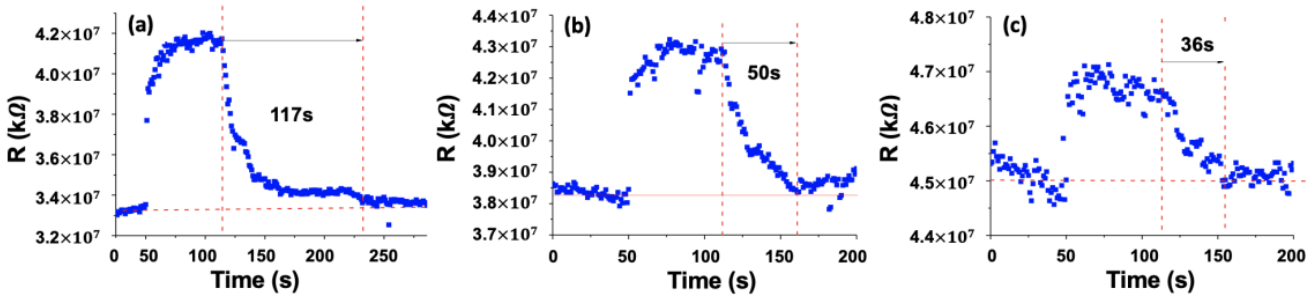

Figure 10. Exposure of gCN sensor device at 1000 ppm of CO_2 at (**a**) 30 °C, (**b**) 35 °C and (**c**) 40 °C.

From the plots of Figure 10, the recovery time as a function of temperature indicates the shortest recovery time of ~36 s achieved at 40 °C, while higher recovery times were registered at 30 °C and 35 °C, at ~117 s and ~50 s, respectively.

Hence, in the following, all our sensing tests were carried out with a 120 s dwell interval, which corresponds to a recovery time of 36 s achieved at 40 °C. A good recovery time was already reported to be considered as an important indicator of a high-performing gas sensor [50–53]. In this sense, the gCN nanosheets were tested for CO_2 detection to evaluate their stability, sensitivity and response. The gCN device was then exposed cyclically to three CO_2 concentrations at 40 °C—200, 600 and 1000 ppm—each for 60 s and maintained at 120 s as dwell time. To monitor the gCN response, a voltage sweep of 2 V at a 0.1 V step was conducted, and the change of the gCN resistance during the CO_2 exposition was collected. The result is illustrated in Figure 11.

As can be seen in Figure 11, for all the three concentrations, the gCN device showed a very fast response of about 730 ms once in contact with CO_2 and a very good recovery time of about 62 s, especially at the lower CO_2 concentration of 200 ppm. These results indicate the high CO_2 reactivity of the elaborated gCN device, as predicted by the adsorption energy calculations.

Moreover, to examine the sensitivity, we exposed (two cycles) the gCN device to CO_2, successively using the following concentrations: 200 ppm, 600 ppm and 1000 ppm. The sensor response is presented in Figure 12.

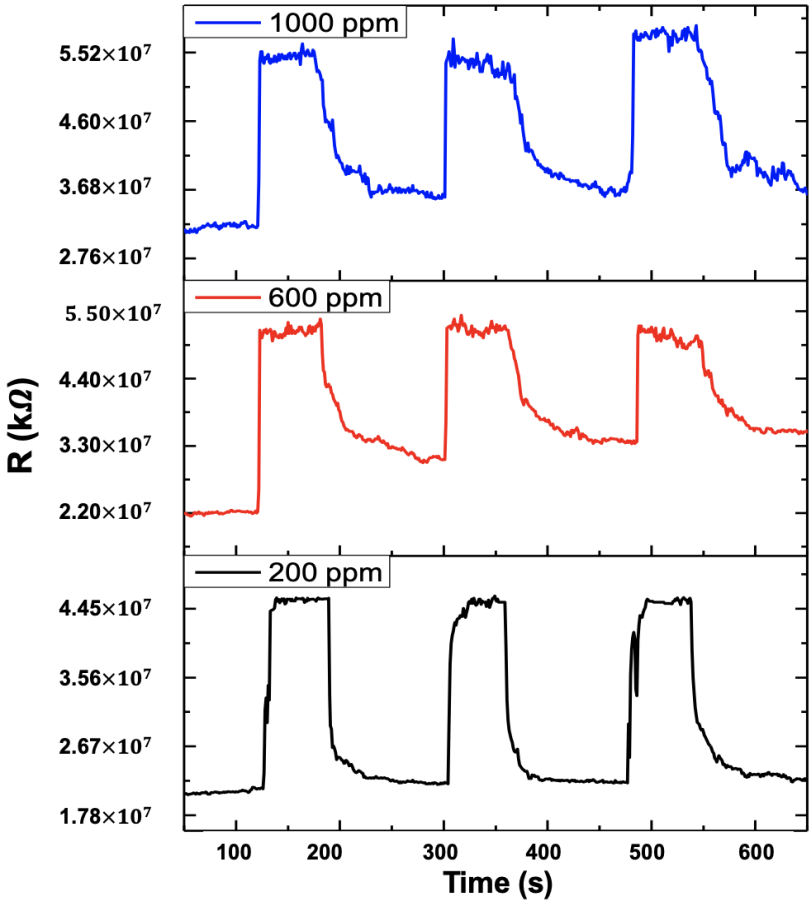

Figure 11. Relative responsiveness of the gCN sensor cyclic exposition to different CO_2 concentrations at 40 °C.

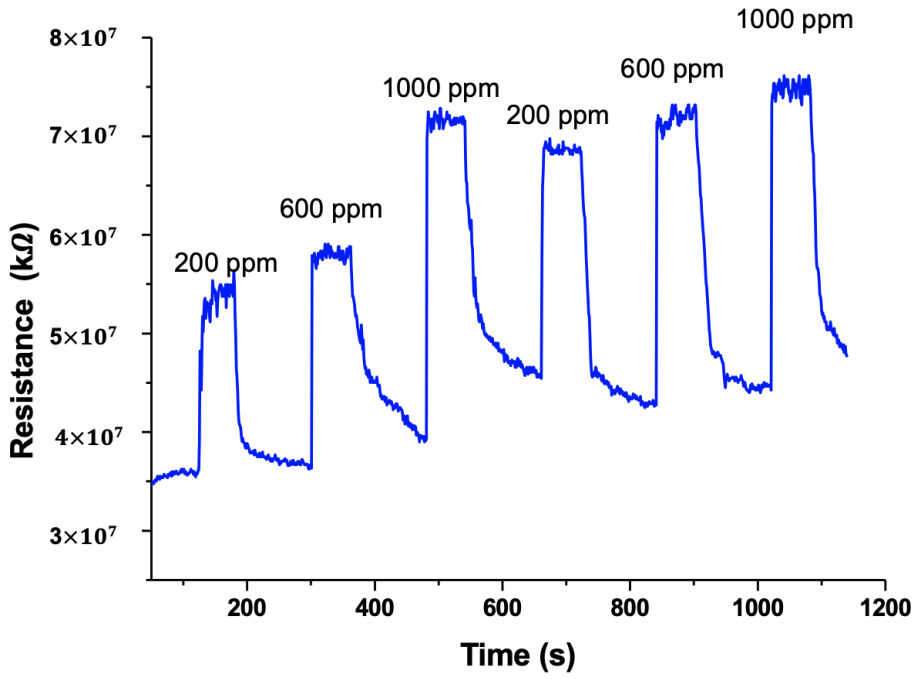

Figure 12. Two cycles of exposure of gCN sensor to CO_2 at 200, 600 and 1000 ppm concentrations at 40 °C.

In this test, the device was repeatedly exposed to gas pulses for 60 s at each concentration, separated by periods of 120 s where the CO_2 stream was cut. The resulting resistance of the device gradually increased with increasing CO_2 gas concentrations. For instance, 5.26×10^7, 5.85×10^7 and 7.17×10^7 kΩ corresponded to 200, 600 and 1000 ppm CO_2 in the first cycle and 6.86×10^7, 7.19×10^7 and 7.50×10^7 kΩ in the second cycle, respectively. This increase in the resistance demonstrates that the gCN device exhibited a very good sensitivity to CO_2 concentration changes.

5. Conclusions

gCN nanosheets were successfully fabricated by the thermal polycondensation of thiourea. The experimental and theoretical investigations have demonstrated an indirect band gap of approximately 2.47 eV and 2.72 eV for bulk and monolayer gCN, respectively. The elaborated gCN was then deposited by spray coating and tested for CO_2 gas sensing. We have evaluated the adsorption of CO_2 into the gas sensor at −0.59 eV, highlighting the very good affinity of gCN nanosheets to CO_2 molecules. The sensing tests revealed that the gCN-based gas sensor has a high CO_2 detection capability of a few hundreds of ppm, high sensitivity and a fast recovery time of 36 s recorded at 40 °C. These findings are expected to provide insights for the low-cost incorporation of gCN to develop very promising, scalable and high-performance gas sensor devices.

Author Contributions: A.K. and M.J. conceived the study; A.K., M.B., E.M.R. and M.L. carried out the experimental and theoretical investigations; A.K., M.B., B.L. and M.J. analyzed the data. All authors contributed equally to writing, editing and reviewing the manuscript. All authors have read and agreed to the published version of the manuscript.

Funding: This research received no external funding.

Data Availability Statement: Data would be made available upon request to the corresponding author.

Acknowledgments: This work is a research collaboration between the University of Picardie Jules Verne (UPJV) and Moroccan Foundation for Advanced Science, Innovation and Research (MAScIR).

Conflicts of Interest: The authors declare no competing interest.

References

1. Yadav, P.; Usha, K.; Singh, B. *Chapter 10—Air Pollution Mitigation and Global Dimming: A Challenge to Agriculture under Changing Climate*; Shanker, A.K., Shanker, C., Anand, A., Maheswari, M., Eds.; Academic Press: Cambridge, MA, USA, 2022; pp. 271–298, ISBN 978-0-12-816091-6.
2. Sikorska, P.E. The need for legal regulation of global emissions from the aviation industry in the context of emerging aerospace vehicles. *Int. Comp. Jurisprud.* **2015**, *1*, 133–142. [CrossRef]
3. Donarelli, M.; Ottaviano, L. 2d materials for gas sensing applications: A review on graphene oxide, mos2, ws2 and phosphorene. *Sensors* **2018**, *18*, 3638. [CrossRef] [PubMed]
4. Liu, X.; Ma, T.; Pinna, N.; Zhang, J. Two-Dimensional Nanostructured Materials for Gas Sensing. *Adv. Funct. Mater.* **2017**, *27*, 1702168. [CrossRef]
5. Mouloua, D.; Kotbi, A.; Deokar, G.; Kaja, K.; El Marssi, M.; EL Khakani, M.A.; Jouiad, M. Recent Progress in the Synthesis of MoS2 Thin Films for Sensing, Photovoltaic and Plasmonic Applications: A Review. *Materials* **2021**, *14*, 3283. [CrossRef] [PubMed]
6. Zhu, B.; Zhang, L.; Xu, D.; Cheng, B.; Yu, J. Adsorption investigation of CO_2 on g-C_3N_4 surface by DFT calculation. *J. CO2 Util.* **2017**, *21*, 327–335. [CrossRef]
7. Hang, N.T.; Zhang, S.; Yang, W. Efficient exfoliation of g-C_3N_4 and NO_2 sensing behavior of graphene/g-C_3N_4 nanocomposite. *Sens. Actuators B Chem.* **2017**, *248*, 940–948. [CrossRef]
8. Zuo, H.W.; Lu, C.H.; Ren, Y.R.; Li, Y.; Zhang, Y.F.; Chen, W.K. Pt_4 clusters supported on monolayer graphitic carbon nitride sheets for oxygen adsorption: A first-principles study. *Wuli Huaxue Xuebao/Acta Phys. Chim. Sin.* **2016**, *32*, 1183–1190. [CrossRef]
9. Song, H.; Liu, L.; Wang, H.; Feng, B.; Xiao, M.; Tang, Y.; Qu, X.; Gai, H.; Huang, T. Adjustment of the band gap of co-doped KCl/NH_4Cl/g-C_3N_4 for enhanced photocatalytic performance under visible light. *Mater. Sci. Semicond. Process.* **2021**, *128*, 105757. [CrossRef]
10. Iqbal, W.; Qiu, B.; Lei, J.; Wang, L.; Zhang, J.; Anpo, M. One-step large-scale highly active g-C_3N_4 nanosheets for efficient sunlight-driven photocatalytic hydrogen production. *Dalt. Trans.* **2017**, *46*, 10678–10684. [CrossRef]

11. Basharnavaz, H.; Habibi-Yangjeh, A.; Kamali, S.H. A first-principle investigation of NO_2 adsorption behavior on Co, Rh, and Ir-embedded graphitic carbon nitride: Looking for highly sensitive gas sensor. *Phys. Lett. Sect. A Gen. At. Solid State Phys.* **2020**, *384*, 126057. [CrossRef]
12. Liu, X.; Kang, W.; Zeng, W.; Zhang, Y.; Qi, L.; Ling, F.; Fang, L.; Chen, Q.; Zhou, M. Structural, electronic and photocatalytic properties of g-C_3N_4 with intrinsic defects: A first-principles hybrid functional investigation. *Appl. Surf. Sci.* **2020**, *499*, 143994. [CrossRef]
13. Ji, Y.; Dong, H.; Lin, H.; Zhang, L.; Hou, T.; Li, Y. Heptazine-based graphitic carbon nitride as an effective hydrogen purification membrane. *RSC Adv.* **2016**, *6*, 52377–52383. [CrossRef]
14. Wu, H.Z.; Liu, L.M.; Zhao, S.J. The effect of water on the structural, electronic and photocatalytic properties of graphitic carbon nitride. *Phys. Chem. Chem. Phys.* **2014**, *16*, 3299–3304. [CrossRef] [PubMed]
15. Jia, L.; Zhang, H.; Wu, P.; Liu, Q.; Yang, W.; He, J.; Liu, C.; Jiang, W. Graphite-like C3N4-coated transparent superhydrophilic glass with controllable superwettability and high stability. *Appl. Surf. Sci.* **2020**, *532*, 147309. [CrossRef]
16. Mohammadi, I.; Zeraatpisheh, F.; Ashiri, E.; Abdi, K. Solvothermal synthesis of g-C_3N_4 and ZnO nanoparticles on TiO_2 nanotube as photoanode in DSSC. *Int. J. Hydrogen Energy* **2020**, *45*, 18831–18839. [CrossRef]
17. Ravichandran, K.; Kalpana, K.; Mohamed Ibrahim, M.; Shantha Seelan, K. Effect of source material of g-C_3N_4 on the photocatalytic activity of ZnO/g-C_3N_4 thin film coated on stainless steel mesh substrate. *Mater. Today Proc.* **2020**, *48*, 207–215. [CrossRef]
18. Mohamed, N.A.; Safaei, J.; Ismail, A.F.; Jailani, M.F.A.M.; Khalid, M.N.; Noh, M.F.M.; Aadenan, A.; Nasir, S.N.S.; Sagu, J.S.; Teridi, M.A.M. The influences of post-annealing temperatures on fabrication graphitic carbon nitride, (g-C_3N_4) thin film. *Appl. Surf. Sci.* **2019**, *489*, 92–100. [CrossRef]
19. Kotbi, A.; Imran, M.; Kaja, K.; Rahaman, A.; Ressami, E.M.; Lejeune, M.; Lakssir, B.; Jouiad, M. Graphene and g-C_3N_4-Based Gas Sensors. *J. Nanotechnol.* **2022**, *2022*, 9671619. [CrossRef]
20. Zinin, P.V.; Ming, L.-C.; Sharma, S.K.; Khabashesku, V.N.; Liu, X.; Hong, S.; Endo, S.; Acosta, T. Ultraviolet and near-infrared Raman spectroscopy of graphitic C_3N_4 phase. *Chem. Phys. Lett.* **2009**, *472*, 69–73. [CrossRef]
21. Bormett, R.W.; Asher, S.A.; Witowski, R.E.; Partlow, W.D.; Lizewski, R.; Pettit, F. Ultraviolet Raman spectroscopy characterizes chemical vapor deposition diamond film growth and oxidation. *J. Appl. Phys.* **1995**, *77*, 5916–5923. [CrossRef]
22. Lin, L.; Ou, H.; Zhang, Y.; Wang, X. Tri-s-triazine-Based Crystalline Graphitic Carbon Nitrides for Highly Efficient Hydrogen Evolution Photocatalysis. *ACS Catal.* **2016**, *6*, 3921–3931. [CrossRef]
23. Wu, J.; Ji, X.; Yuan, X.; Zhao, Z.; Li, Y.; Wen, B.; Zhang, H.; Yu, D.; Zhao, Y.; Tian, Y. Regulating Polymerization in Graphitic Carbon Nitride To Improve Photocatalytic Activity. *Chem. Mater.* **2019**, *31*, 9188–9199. [CrossRef]
24. Li, H.; Jin, C.; Wang, Z.; Liu, Y.; Wang, P.; Zheng, Z.; Whangbo, M.H.; Kou, L.; Li, Y.; Dai, Y.; et al. Effect of the intra- and inter-triazine N-vacancies on the photocatalytic hydrogen evolution of graphitic carbon nitride. *Chem. Eng. J.* **2019**, *369*, 263–271. [CrossRef]
25. Ferrari, A.C.; Robertson, J.; Ferrari, A.C.; Robertson, J. Raman spectroscopy of amorphous, nanostructured, diamond-like carbon, and nanodiamond. *Philos. Trans. R. Soc. Lond. Ser. A Math. Phys. Eng. Sci.* **2004**, *362*, 2477–2512. [CrossRef] [PubMed]
26. Ferrari, A.C.; Robertson, J. Interpretation of Raman spectra of disordered and amorphous carbon. *Phys. Rev. B* **2000**, *61*, 14095–14107. [CrossRef]
27. Kotbi, A.; Hartiti, B.; Ridah, A.; Thevenin, P. Characteristics of CuInS2 thin films synthesizes by chemical spray pyrolysis. *Opt. Quantum Electron.* **2016**, *48*, 75. [CrossRef]
28. Wang, H.; Zhang, X.; Xie, J.; Zhang, J.; Ma, P.; Pan, B.; Xie, Y. Structural distortion in graphitic-C3N4 realizing an efficient photoreactivity. *Nanoscale* **2015**, *7*, 5152–5156. [CrossRef]
29. Pareek, S.; Quamara, J.K. Dielectric and optical properties of graphitic carbon nitride–titanium dioxide nanocomposite with enhanced charge seperation. *J. Mater. Sci.* **2018**, *53*, 604–612. [CrossRef]
30. Dong, F.; Zhao, Z.; Xiong, T.; Ni, Z.; Zhang, W.; Sun, Y.; Ho, W. In Situ Construction of g-C_3N_4/g-C_3N_4 Metal-Free Heterojunction for Enhanced Visible-Light Photocatalysis. *ACS Appl. Mater. Interfaces* **2013**, *5*, 11392–11401. [CrossRef]
31. Liu, J. Effect of phosphorus doping on electronic structure and photocatalytic performance of g-C_3N_4: Insights from hybrid density functional calculation. *J. Alloys Compd.* **2016**, *672*, 271–276. [CrossRef]
32. Yu, W.; Xu, D.; Peng, T. Enhanced photocatalytic activity of g-C_3N_4 for selective CO_2 reduction to CH_3OH via facile coupling of ZnO: A direct Z-scheme mechanism. *J. Mater. Chem. A* **2015**, *3*, 19936–19947. [CrossRef]
33. Li, L.; Huang, Z.; Li, Z.; Li, H.; Wang, A. Defect-rich porous g-C_3N_4 nanosheets photocatalyst with enhanced photocatalytic activity. *J. Mater. Sci. Mater. Electron.* **2021**, *32*, 6465–6474. [CrossRef]
34. Liang, Q.; Li, Z.; Huang, Z.H.; Kang, F.; Yang, Q.H. Holey Graphitic Carbon Nitride Nanosheets with Carbon Vacancies for Highly Improved Photocatalytic Hydrogen Production. *Adv. Funct. Mater.* **2015**, *25*, 6885–6892. [CrossRef]
35. Azofra, L.M.; MacFarlane, D.R.; Sun, C. A DFT study of planar: Vs. corrugated graphene-like carbon nitride (g-C_3N_4) and its role in the catalytic performance of CO_2 conversion. *Phys. Chem. Chem. Phys.* **2016**, *18*, 18507–18514. [CrossRef] [PubMed]
36. Ding, K.; Wen, L.; Huang, M.; Zhang, Y.; Lu, Y.; Chen, Z. How does the B,F-monodoping and B/F-codoping affect the photocatalytic water-splitting performance of g-C_3N_4? *Phys. Chem. Chem. Phys.* **2016**, *18*, 19217–19226. [CrossRef]
37. Wang, Y.; Tian, Y.; Yan, L.; Su, Z. DFT Study on Sulfur-Doped g-C_3N_4 Nanosheets as a Photocatalyst for CO_2 Reduction Reaction. *J. Phys. Chem. C* **2018**, *122*, 7712–7719. [CrossRef]

38. Yao, Q.; Lu, M.; Du, Y.; Wu, F.; Deng, K.; Kan, E. Designing half-metallic ferromagnetism by a new strategy: An example of superhalogen modified graphitic C_3N_4. *J. Mater. Chem. C* **2018**, *6*, 1709–1714. [CrossRef]
39. Zhang, X.; Xie, X.; Wang, H.; Zhang, J.; Pan, B.; Xie, Y. Enhanced photoresponsive ultrathin graphitic-phase C_3N_4 nanosheets for bioimaging. *J. Am. Chem. Soc.* **2013**, *135*, 18–21. [CrossRef]
40. Meng, J.; Pei, J.; He, Z.; Wu, S.; Lin, Q.; Wei, X.; Li, J.; Zhang, Z. Facile synthesis of g-C_3N_4 nanosheets loaded with WO_3 nanoparticles with enhanced photocatalytic performance under visible light irradiation. *RSC Adv.* **2017**, *7*, 24097–24104. [CrossRef]
41. Liu, J.; Hua, E. High Photocatalytic Activity of Heptazine-Based g-C_3N_4/SnS_2 Heterojunction and Its Origin: Insights from Hybrid DFT. *J. Phys. Chem. C* **2017**, *121*, 25827–25835. [CrossRef]
42. Opoku, F.; Govender, K.K.; van Sittert, C.G.C.E.; Govender, P.P. Insights into the photocatalytic mechanism of mediator-free direct Z-scheme g-C_3N_4/Bi_2MoO_6(010) and g-C_3N_4/Bi_2WO_6(010) heterostructures: A hybrid density functional theory study. *Appl. Surf. Sci.* **2018**, *427*, 487–498. [CrossRef]
43. Xu, L.; Huang, W.Q.; Wang, L.L.; Tian, Z.A.; Hu, W.; Ma, Y.; Wang, X.; Pan, A.; Huang, G.F. Insights into enhanced visible-light photocatalytic hydrogen evolution of g-C_3N_4 and highly reduced graphene oxide composite: The role of oxygen. *Chem. Mater.* **2015**, *27*, 1612–1621. [CrossRef]
44. Liu, J.; Cheng, B.; Yu, J. A new understanding of the photocatalytic mechanism of the direct Z-scheme g-C_3N_4/TiO_2 heterostructure. *Phys. Chem. Chem. Phys.* **2016**, *18*, 31175–31183. [CrossRef] [PubMed]
45. Chen, X.; Zhou, C.; Zhao, W.; He, H.; Li, R.; Zou, W. Hybrid triazine-based graphitic carbon nitride and molybdenum disulfide bilayer with and without Li/Mg intercalation: Structural, electronic and optical properties. *Comput. Mater. Sci.* **2017**, *134*, 84–92. [CrossRef]
46. Ruan, L.; Xu, G.; Gu, L.; Li, C.; Zhu, Y.; Lu, Y. The physical properties of Li-doped g-C_3N_4 monolayer sheet investigated by the first-principles. *Mater. Res. Bull.* **2015**, *66*, 156–162. [CrossRef]
47. Deokar, G.; Casanova-Cháfer, J.; Rajput, N.S.; Aubry, C.; Llobet, E.; Jouiad, M.; Costa, P.M.F.J. Wafer-scale few-layer graphene growth on Cu/Ni films for gas sensing applications. *Sens. Actuators B Chem.* **2020**, *305*, 127458. [CrossRef]
48. Zhang, Y.H.; Chen, Y.B.; Zhou, K.G.; Liu, C.H.; Zeng, J.; Zhang, H.L.; Peng, Y. Improving gas sensing properties of graphene by introducing dopants and defects: A first-principles study. *Nanotechnology* **2009**, *20*, 185504. [CrossRef]
49. Dervieux, E.; Théron, M.; Uhring, W. Carbon Dioxide Sensing-Biomedical Applications to Human Subjects. *Sensors* **2022**, *22*, 188. [CrossRef]
50. Li, W.; Zhang, Y.; Long, X.; Cao, J.; Xin, X.; Guan, X.; Peng, J.; Zheng, X. Gas Sensors Based on Mechanically Exfoliated MoS_2 Nanosheets for Room-Temperature NO_2 Detection. *Sensors* **2019**, *19*, 2123. [CrossRef]
51. Presmanes, L.; Thimont, Y.; Chapelle, A.; Blanc, F.; Talhi, C.; Bonningue, C.; Barnabé, A.; Menini, P.; Tailhades, P. Highly sensitive sputtered zno:Ga thin films integrated by a simple stencil mask process on microsensor platforms for sub-ppm acetaldehyde detection. *Sensors* **2017**, *17*, 1055. [CrossRef]
52. Presmanes, L.; Thimont, Y.; El Younsi, I.; Chapelle, A.; Blanc, F.; Talhi, C.; Bonningue, C.; Barnabé, A.; Menini, P.; Tailhades, P. Integration of P-Cuo thin sputtered layers onto microsensor platforms for gas sensing. *Sensors* **2017**, *17*, 1409. [CrossRef] [PubMed]
53. Zhang, X.; Wang, Y.; Luo, G.; Xing, M. Two-Dimensional Graphene Family Material. *Sensors* **2019**, *19*, 2966. [CrossRef] [PubMed]